

MobileFetalCLIP: Selective Repulsive Knowledge Distillation for Mobile Fetal Ultrasound Analysis

Numan Saeed^{1*}, Fadillah Adamsyah Maani¹, and Mohammad Yaqub¹

Computer Vision Department, Mohamed bin Zayed University of Artificial Intelligence,
Abu Dhabi, UAE

Abstract. Fetal ultrasound AI could transform prenatal care in low-resource settings, yet current foundation models exceed 300M visual parameters, precluding deployment on point-of-care devices. Standard knowledge distillation fails under such extreme capacity gaps ($\approx 26\times$), as compact students waste capacity mimicking architectural artifacts of oversized teachers. We introduce **Selective Repulsive Knowledge Distillation**, which decomposes contrastive KD into diagonal and off-diagonal components: matched pair alignment is preserved while the off-diagonal weight decays into negative values, repelling the student from the teacher’s inter-class confusions and forcing discovery of architecturally native features. Our 11.4M parameter student surpasses the 304M-parameter FetalCLIP teacher on zero-shot HC18 biometry validity (**88.6%** vs. 83.5%) and brain sub-plane F1 (**0.784** vs. 0.702), while running at 1.6 ms on iPhone 16 Pro, enabling real-time assistive AI on handheld ultrasound devices. Our code and models are publicly available at <https://github.com/numanai/MobileFetalCLIP>.

Keywords: Knowledge distillation · Fetal ultrasound · Vision-language models · Mobile AI · Repulsive regularisation

1 Introduction

Fetal ultrasound is the primary modality for monitoring fetal wellbeing, spanning standard plane classification [3, 5], biometric measurement [24], and congenital heart disease screening [2]. Deploying AI assistance at the point of care is clinically impactful, particularly in low-resource settings where ultrasound expertise remains limited [26] and AI-driven mobile solutions are emerging to bridge the gap [9, 23]. Recent vision-language foundation models such as FetalCLIP [17] demonstrate compelling zero-shot capabilities across these tasks by pretraining on large-scale clinical image-caption pairs. However, FetalCLIP’s ViT-L/14 image encoder alone contains ≈ 304 M parameters (427M parameters for the full model), making it unsuitable for point-of-care ultrasound (POCUS) devices such as handheld probes and tablet-based platforms.

Knowledge distillation (KD) [11] provides a natural pathway: train a compact student to mimic a large teacher. For vision-language models, prior work such as

* Corresponding author: numan.saeed@mbzuai.ac.ae

TinyCLIP [34] and CLIP-KD [35] demonstrates that distilling CLIP-family models preserves zero-shot generalisation. However, these approaches target general-domain vision and assume moderate teacher-student capacity gaps. When the gap is large, as in our setting where the teacher has $\approx 26\times$ more visual parameters, Cho and Hariharan [7] show that standard KD degrades, and Stanton *et al.* [25] demonstrate that higher fidelity to the teacher does not guarantee better student accuracy. We argue that the core issue is *architectural incommensurability*: the teacher’s off-diagonal (non-target) similarity structure is shaped in part by ViT-L’s global self-attention, whereas a convolution-attention hybrid student such as FastViT must allocate capacity to approximating patterns it cannot naturally represent.

In this work, we distil FetalCLIP into MobileFetalCLIP (Figure 1), a mobile model with a FastViT image encoder [1, 30, 31] (11.4M visual parameters, $26\times$ fewer than the teacher). We extend the distillation schedule to negative minimum ratios ($r < 0$), at which point the KD weight crosses zero and the objective *inverts*: instead of attracting the student toward the teacher’s inter-class similarity structure, it repels the student away from it, using the teacher’s confusion patterns as a structured signal for where the student should build sharper boundaries with its own architectural strengths. Building on the insight from Decoupled KD [39] that target-class and non-target-class knowledge serve different roles, we decompose the contrastive KD loss into diagonal (matched-pair) and off-diagonal (non-target) components, applying repulsion selectively to the off-diagonal components while protecting matched-pair alignment. We term this **Selective Repulsive KD**; the selective repulsion forces the student to discover *architecturally native* features, *i.e.* compact discriminative cues suited to FastViT’s convolutional-attention hybrid design rather than replications of ViT-L’s global self-attention patterns (Secs. 4.6 and 5).

Our key finding is that Selective Repulsive KD outperforms all standard KD baselines and surpasses the teacher on key zero-shot evaluation axes. Compared to the standard logit KD baseline, Selective Repulsive KD improves HC18 biometry validity from 79.4% to **88.6%** (+9.2 pp) and zero-shot brain sub-plane F1 from 0.715 to **0.784** (+6.9 pp). With $26\times$ fewer visual encoder parameters, MobileFetalCLIP surpasses the FetalCLIP teacher in zero-shot HC18 biometry validity (88.6% vs. 83.5%, +5.1 pp) and zero-shot brain sub-plane F1 (0.784 vs. 0.702, +8.2 pp), while maintaining competitive 5-plane classification (0.946 vs. 0.973). Linear probing confirms that frozen MobileFetalCLIP features retain 97–98% of the teacher’s downstream performance (Sec. 4.7), indicating that the capacity gap primarily limits raw feature information while Selective Repulsive KD recovers and even improves the relational structure that zero-shot evaluation probes. Analysis via embedding geometry and logit distributions (Sec. 4.6) reveals the mechanism: Selective Repulsive KD produces *structured decorrelation*, yielding well-separated, confident representations that are systematically different from the teacher’s.

Selective Repulsive KD connects to Decoupled KD [39], decorrelation-based learning [32, 36], and confidence regularisation [20], but occupies a distinct position

among these paradigms; we formalise this relationship in Sec. 3.5 and validate it empirically in Sec. 4.4. Our main **contributions** are:

- We propose **Selective Repulsive Knowledge Distillation**, an architecture- and domain-agnostic methodology which decomposes contrastive KD into diagonal (matched-pair) and off-diagonal (non-target) components. By applying repulsion selectively to the off-diagonal while preserving matched-pair alignment, it provides a general framework for distilling over-parameterised foundation models into highly compact students.
- We introduce MobileFetalCLIP, a mobile-scale vision-language model for fetal ultrasound that surpasses the FetalCLIP teacher in zero-shot HC18 biometry validity and brain sub-plane F1 at $26\times$ fewer visual encoder parameters, while retaining 97–98% of linear probing performance (Tabs. 1 and 5).
- We provide mechanistic analysis via embedding geometry, logit distributions, and controlled ablations, demonstrating that Selective Repulsive KD produces structured decorrelation and that the teacher’s logit geometry is essential as a directional signal (Secs. 3.5 and 4.6).

2 Related Work

Vision-Language Pretraining. CLIP [21] demonstrated that contrastive pretraining on image-text pairs yields transferable zero-shot representations. Subsequent work refined the objective (SigLIP [37]), scaling laws (OpenCLIP [6,13]), and efficiency (MobileCLIP [1,31]). Our student backbone extends MobileCLIP with multi-modal reinforced training, yielding strong accuracy-per-parameter trade-offs via a FastViT image encoder [30].

Medical Vision-Language Models. MedCLIP [33], BiomedCLIP [38], and UniMed-CLIP [14] adapt CLIP to the medical domain using broad biomedical corpora spanning multiple imaging modalities. CheXzero [29] demonstrates that modality-specific CLIP pretraining on chest X-rays achieves expert-level zero-shot pathology detection, confirming the importance of domain specificity. None of these models transfer effectively to fetal ultrasound (Tab. 1). FetalCLIP [17] is the first VLM specialised for fetal ultrasound, achieving state-of-the-art across plane classification, biometry, and congenital heart disease detection. However, it employs a 304M-parameter ViT-Large model as its image encoder, limiting its suitability for resource-constrained deployment scenarios such as POCUS and mobile devices.

Knowledge Distillation and the Capacity Gap. Hinton *et al.* [11] showed that soft targets carry rich inter-class structure; FitNets [22] extended this to intermediate features; CRD [28] established contrastive objectives for distillation; RKD [19] distilled relational structure between samples. For CLIP models, CLIP-KD [35] studied logit, feature, and combined strategies; TinyCLIP [34] used weight inheritance, though this requires the student to be a pruned version of the teacher,

which is inapplicable when teacher and student differ architecturally. Zhao *et al.* [39] showed in Decoupled KD that independently weighting target-class and non-target-class components improves distillation; we adapt this decomposition to the contrastive $N \times N$ setting and extend it to negative weights.

Crucially, distillation degrades with increasing capacity gap [7, 18, 25]: larger teachers can produce worse students, and exact KL-matching destabilises under strong teachers [12, 27]. Conversely, Furlanello *et al.* [8] showed re-distilled students can surpass their teacher. Prior approaches either bridge the gap via intermediate models [18], relax the objective [12, 27], or require architectural correspondence [34]. Selective Repulsive KD takes an orthogonal approach: we exploit the teacher’s confusion structure as a directional signal, inverting the off-diagonal objective to push the student toward architecturally native representations.

Regularisation and Decorrelation. Barlow Twins [36] showed that decorrelating representation dimensions prevents collapse and improves generalisation; Wang and Isola [32] formalised alignment and uniformity as the two desiderata of contrastive learning. Building on these principles, we subsequently measure alignment and uniformity to characterise the decorrelation mechanism of our repulsive objective (Sec. 4.6). Kim *et al.* [15] demonstrated that negative learning, where the model learns what a class is *not*, can be more robust than positive learning, providing a conceptual parallel to our teacher-informed repulsion. Pereyra *et al.* [20] showed that penalising overconfident predictions improves generalisation. Our repulsive regime is superficially similar but fundamentally differs in its use of the teacher’s logit geometry as a directional signal; we formalise this distinction in Sec. 3.5.

3 Method

3.1 Preliminary: CLIP Contrastive Learning

Given a batch of N image-text pairs $\{(x_i, c_i)\}_{i=1}^N$, CLIP [21] trains image encoder f_I and text encoder f_T by maximising the cosine similarity between paired embeddings and minimising it for non-paired ones:

$$\mathcal{L}_{\text{CLIP}} = -\frac{1}{2N} \sum_{i=1}^N \left[\log \frac{e^{s_{ii}/\tau}}{\sum_{j=1}^N e^{s_{ij}/\tau}} + \log \frac{e^{s_{ii}/\tau}}{\sum_{j=1}^N e^{s_{ji}/\tau}} \right], \quad (1)$$

where $s_{ij} = f_I(x_i)^\top f_T(c_j)$ and τ is a learned temperature (inverse logit scale).

3.2 Logit Knowledge Distillation

Following CLIP-KD [35], we align the $N \times N$ similarity logit matrices of student and teacher. The teacher (FetalCLIP, ViT-L/14) is frozen; the student (FastViT) is trained. Given student logit matrix S^S and teacher logit matrix S^T , we soften

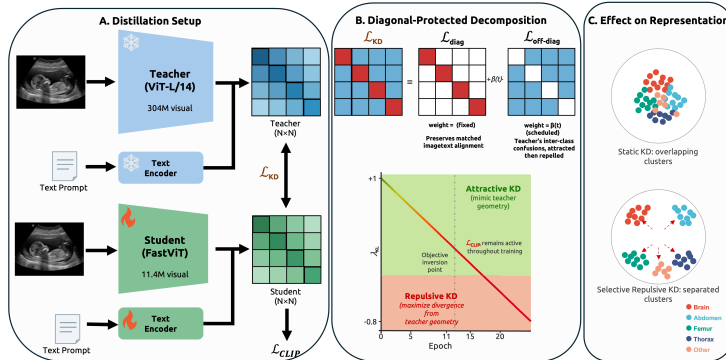


Fig. 1: Overview of the MobileFetalCLIP framework. **(A)** Distillation setup: a frozen FetalCLIP teacher (ViT-L/14, 304M visual params) produces an $N \times N$ similarity matrix; a lightweight FastViT student (11.4M visual params) is trained via $\mathcal{L}_{\text{CLIP}}$ and \mathcal{L}_{KD} . **(B)** Attraction-to-repulsion dynamics: the off-diagonal weight $\beta(t)$ decays from β_0 into negative values; the diagonal weight $\mathcal{L}_{\text{diag}}$ remains fixed, preserving matched-pair alignment throughout training. **(C)** Outcome: Selective Repulsive KD produces structured decorrelation, resulting in better cluster separation and a higher HC18 validity rate and brain sub-plane F1 with $26\times$ fewer visual parameters.

only the teacher with KD temperature τ_{KD} while keeping the student at native scale:

$$p_i^T = \text{softmax}\left(\frac{S_{i,:}^T}{\tau_{\text{KD}}}\right), \quad q_i^S = \text{softmax}(S_{i,:}^S), \quad (2)$$

where p_i^T and q_i^S denote the row-wise softmax distributions of teacher and student, respectively. The symmetric logit KD loss averages the image-to-text ($I \rightarrow T_x$) and text-to-image ($T_x \rightarrow I$) directions, where T_x here denotes text (not teacher):

$$\mathcal{L}_{\text{KD}} = \frac{1}{2} [\mathcal{H}(p^T, q^S)_{I \rightarrow T_x} + \mathcal{H}(p^T, q^S)_{T_x \rightarrow I}], \quad (3)$$

where $\mathcal{H}(p, q) = -\sum_j p_j \log q_j$ is the cross-entropy, equivalent to $\text{KL}(p^T \| q^S)$ up to additive teacher-entropy constants. We apply temperature only to the teacher (student unscaled, no T^2 correction); details are in supplementary § 1.3.

3.3 Linear Decay Schedule and Repulsive KD

The total training objective is:

$$\mathcal{L} = \mathcal{L}_{\text{CLIP}} + \lambda_{\text{KL}}(t) \cdot \mathcal{L}_{\text{KD}}, \quad (4)$$

where $\lambda_{\text{KL}}(t)$ follows a linear schedule parameterised by initial weight λ_0 , total training epochs \mathcal{S} (distinct from temperature τ), and minimum ratio r :

$$\lambda_{\text{KL}}(t) = \lambda_0 \cdot \left(1 - \frac{t}{\mathcal{S}}(1 - r)\right). \quad (5)$$

For $r \geq 0$, λ_{KL} decays to a positive floor $\lambda_0 r$, corresponding to standard KD that weakens over time. **When $r < 0$, λ_{KL} eventually becomes negative.** At this point the gradient of $\lambda_{\text{KL}}(t) \cdot \mathcal{L}_{\text{KD}}$ *inverts*: instead of minimising KL divergence from the teacher, the objective *maximises* it, actively repelling the student’s similarity distribution away from the teacher’s. We call this the **Repulsive KD** regime. The off-diagonal entries of the teacher’s similarity matrix encode inter-class confusions that are partly architectural: patterns arising from ViT-L’s global self-attention rather than intrinsic visual ambiguity alone (confirmed empirically in Sec. 4.6). A convolutional student forced to replicate these patterns wastes capacity on confusion structures it cannot naturally represent; repulsion frees it to resolve these confusions using its architecturally native local-texture and multi-scale features.

The training process proceeds through three phases (Figure 1B):

1. **Attractive phase** ($\lambda_{\text{KL}} > 0$): Standard KD, where the student absorbs domain knowledge from the teacher’s similarity structure.
2. **Transition** ($\lambda_{\text{KL}} \approx 0$): Near the zero-crossing, the KD term contributes negligibly and the student is driven primarily by $\mathcal{L}_{\text{CLIP}}$.
3. **Repulsive phase** ($\lambda_{\text{KL}} < 0$): The gradient inverts, pushing the student to resolve inter-class confusions differently from the teacher. Combined with the always-positive $\mathcal{L}_{\text{CLIP}}$ which maintains correct image-text alignment, this forces discovery of architecturally native features suited to FastViT’s convolutional-attention design.

3.4 Selective Repulsive KD: Diagonal-Protected Decomposition

Zhao *et al.* [39] showed that in classification KD, the non-target class component (NCKD) carries the majority of the “dark knowledge” and benefits from independent weighting. We adapt this decomposition to the contrastive setting. In the $N \times N$ similarity matrix, diagonal entries ($i=j$) represent matched image-text pairs (analogous to TCKD), while off-diagonal entries ($i \neq j$) capture non-target similarity structure (analogous to NCKD). We decompose the KD loss:

$$\mathcal{L}_{\text{KD}} = \mathcal{L}_{\text{diag}} + \beta(t) \cdot \mathcal{L}_{\text{off-diag}}, \quad (6)$$

where, for each row of the cross-entropy $\mathcal{H}(p_i^T, q_i^S) = -\sum_j p_{ij}^T \log q_{ij}^S$, we partition the sum into its $j=i$ term ($\mathcal{L}_{\text{diag}}$) and its $j \neq i$ terms ($\mathcal{L}_{\text{off-diag}}$). The diagonal weight is fixed at 1.0 throughout training, preserving correct image-text alignment. The off-diagonal weight $\beta(t)$ follows the same linear schedule as Eq. (5), parameterised by initial value β_0 and minimum ratio r :

$$\beta(t) = \beta_0 \cdot \left(1 - \frac{t}{\mathcal{S}}(1 - r) \right), \quad (7)$$

and is permitted to become negative when $r < 0$. In coupled mode (Eq. (4)), the same schedule applies uniformly to the entire \mathcal{L}_{KD} via $\lambda_{\text{KL}}(t)$; in selective mode, only the off-diagonal component is scheduled while the diagonal remains fixed.

This **diagonal protection** ensures that even during the repulsive phase, the student maintains high-quality matched-pair representations. Only the non-target similarity structure, *i.e.* how the student relates *non-matching* images and texts, is pushed away from the teacher’s pattern.

Following Zhao *et al.*’s finding that upweighting NCKD improves distillation [39], we allow $\beta_0 > 1$ (**NCKD amplification**), which increases the emphasis on non-target structure during the attractive phase before the transition into repulsion. The sensitivity to β_0 is analysed in Sec. 4.4.

3.5 Positioning Among Regularisation Paradigms

Selective Repulsive KD relates to two confidence-modulating strategies, yet differs in directionality: **(i)** confidence penalty [20] pushes toward *uniform* distributions with no notion of which classes to separate; **(ii)** standard KD [11] attracts toward the *teacher’s* distribution, constraining under large capacity gaps; **(iii)** Selective Repulsive KD repels from the teacher’s *non-target* structure while preserving matched-pair alignment. The teacher’s confusion patterns tell the student exactly *which* class pairs to separate; our ablation (Sec. 4.4) confirms that this directionality is essential, as undirected entropy performs comparably to no KD.

3.6 Training Setup

Models. The student uses a FastViT image encoder [1, 30, 31] (11.4M visual parameters, 256×256 input, 512-d embeddings) with a 4-layer text Transformer (75M total parameters). The teacher is FetalCLIP [17] with ViT-L/14 (304M visual parameters, 427M total), frozen throughout training.

Training data. We use the FetalCLIP pretraining corpus [17]: 246,349 fetal ultrasound image-caption pairs comprising routine second-trimester clinical scans from a tertiary hospital with LLM-generated captions and expert-annotated textbook image-caption pairs, served in WebDataset format [4]. We train for 20 epochs with effective batch size 1,024 and $\tau_{\text{KD}} = 5.0$ (following CLIP-KD [35]; the elevated temperature amplifies the repulsive signal once λ_{KL} crosses zero). With the linear schedule (Eq. (5)), the zero crossing occurs at epoch $t^* = \mathcal{S}/(1-r) \approx 11$ for $r = -0.8$.

Augmentation. In KD mode, student and teacher views share the same sampled affine/jitter parameters (coupled augmentation), so compared logit matrices correspond to the same underlying view.

Full details. Complete hyperparameters, optimiser/scheduler settings, precision/distributed setup, and data pipeline details are provided in supplementary § 1.

4 Experiments

4.1 Evaluation Setup

Datasets. We evaluate zero-shot performance on two public benchmarks.

Planes DB [5]: 12,400 fetal ultrasound images from 1,792 patients across two hospitals. We use 8,187 images for 5-plane classification (abdomen, brain, femur, thorax, cervix; excluding the “Other” category) and 2,949 brain images for 3-class brain sub-plane classification (transthalamic, transcerebellum, transventricular). Following FetalCLIP [17], zero-shot evaluation uses the full labelled set rather than introducing an additional train/test partition.

HC18 [10]: 999 head circumference images. We filter to 814 with physiologically plausible HC (100–342 mm, corresponding to 14–40 weeks gestational age). Following FetalCLIP [17], we report *validity rate*: gestational age (GA) is predicted via similarity matching against GA-specific text prompts, and a prediction is *valid* if the true HC falls within the 2.5th–97.5th percentile range of the WHO fetal growth charts [16] for the predicted GA.

Metrics. All metrics are zero-shot. We report the HC18 validity score, the macro-average F1 for 5-plane classification (F1-5Plane), and the macro-average F1 for 3-class brain sub-plane classification (F1-3Brain). We also report F1-all, the macro-average across all fetal-plane classes, computed as $F1\text{-all} = \frac{5 \times F1\text{-5Plane} + 3 \times F1\text{-3Brain}}{8}$. For hyperparameter selection across runs, we use the average of F1-all and the HC18 validity rate (denoted Avg.[‡] in tables); this is *not* an evaluation metric but a run-selection heuristic.

Baselines. We compare against CLIP (ViT-L/14) [21], BiomedCLIP [38], UniMed-CLIP [14], SonoNet [3], and the FetalCLIP teacher [17]; baseline numbers are from Maani *et al.* [17]. The primary distillation baseline is **static logit KD** ($\lambda_{KL}=1.0$), implementing the CLIP-KD [35] symmetric cross-entropy objective. TinyCLIP-style weight inheritance [34] is inapplicable as our student (FastViT) and teacher (ViT-L/14) share no architectural correspondence.

4.2 Main Results

Table 1 reports zero-shot performance on both benchmarks. Without distillation, the student achieves HC18 validity of 71.3% and F1-5Plane of 0.889 from contrastive pretraining alone. Standard logit KD (the CLIP-KD [35] baseline) improves HC18 to 79.4% and F1-5Plane to 0.946, confirming that the teacher provides valuable domain knowledge. However, HC18 validity remains well below the teacher’s 83.5%, consistent with the capacity-gap degradation predicted by Cho and Hariharan [7].

Selective Repulsive KD not only closes this gap but inverts the degradation. With $26\times$ fewer visual parameters, MobileFetalCLIP surpasses the FetalCLIP teacher on HC18 biometry validity (88.6% vs. 83.5%, +5.1 pp) and brain sub-plane F1 (0.784 vs. 0.702, +8.2 pp), while maintaining competitive 5-plane classification (0.946 vs. 0.973). The improvement from CLIP-KD baseline to Selective Repulsive KD is entirely attributable to the distillation strategy, as the architecture and training data are identical.

Table 1: Zero-shot comparison on fetal ultrasound benchmarks. Best student result in **bold**. Static Logit KD implements the CLIP-KD [35] objective (the standard distillation baseline for CLIP models). Avg.[‡]: run-selection heuristic $(F1\text{-all} + HC18\%/100)/2$. †: results from Maani *et al.* [17].

Model	Params	HC18 (%)	F1-5Pl.	F1-3Br.	F1-all	Avg. [‡]
<i>Teacher</i>						
FetalCLIP (ViT-L/14) [†]	427M	83.5	0.973	0.702	0.871	0.853
<i>General VLMs (not fetal-specific)</i>						
CLIP (ViT-L/14) [†]	427M	11.0	0.308	0.206	0.270	0.190
BiomedCLIP (ViT-B/16) [†]	150M	24.0	0.603	0.236	0.466	0.353
UniMed-CLIP (ViT-B/16) [†]	150M	9.0	0.679	0.187	0.495	0.293
<i>Supervised (not zero-shot)</i>						
SonoNet-16 [†]	11M	–	0.827	0.485	0.699	–
<i>MobileFetalCLIP (FastViT, 75M total)</i>						
No KD (CLIP only)	75M	71.3	0.889	0.712	0.823	0.768
Static Logit KD (CLIP-KD baseline)	75M	79.4	0.946	0.715	0.859	0.826
Coupled Repulsive KD ($r=-0.8$)	75M	84.4	0.933	0.763	0.869	0.857
Selective Repulsive KD ($\beta_0=2, r=-0.8$)	75M	88.6	0.946	0.784	0.886	0.886

Table 2: Inference efficiency: visual-encoder parameters, GMACs, and on-device encoder latency (CoreML, fp16, batch 1). Measured on two iPhones to show generational consistency.

Model	Vis. Params	GMACs	iPhone Latency (ms)	
			16 Pro	17 Pro
FetalCLIP (ViT-L/14)	304M	38.9	37.6	31.9
MobileFetalCLIP (FastViT)	11.4M (26×↓)	1.2 (32×↓)	1.6 (24×↓)	1.4 (23×↓)

4.3 Inference Efficiency

Table 2 compares the visual encoder’s computational cost. The student requires 32× fewer multiply-accumulate operations and 26× fewer parameters than the teacher. On an iPhone 16 Pro the encoder runs in 1.6 ms (24× faster than the teacher’s 37.6 ms), corresponding to over 600 frames per second, well beyond the 30–60 fps typical of diagnostic ultrasound. This throughput headroom means the encoder can be embedded in an on-device assistive pipeline for real-time standard-plane identification without interfering with the clinical scanning workflow.

4.4 Ablation Study

Table 3 presents the full ablation. The results reveal a clear progression: **Standard KD helps, but has limits.** Static KD ($\lambda_{KL}=1.0$) improves F1-5Plane from 0.889 to 0.946 and HC18 validity from 71.3% to 79.4%. However, HC18 remains well below the teacher’s 83.5%, and F1-3Brain barely moves (0.712→0.715).

Positive decay and complete abandonment fail. Decaying λ_{KL} to 0.1 degrades HC18 to 74.6%. Complete teacher abandonment ($r=0.0$) is worst among

decay schedules (HC18 73.1%), confirming that the teacher provides essential regularisation.

Confidence penalty is not the answer. The confidence penalty ($\varepsilon=0.1$, HC18 74.9%, F1-3Brain 0.680) performs comparably to no KD, confirming that undirected entropy maximisation cannot substitute for structured teacher guidance.

Feature KD consistently hurts. Adding CLIP-KD-style [35] feature alignment ($\lambda_{\text{feat}}=2000$) to static KD degrades HC18 from 79.4% to 75.9% and F1-3Brain from 0.715 to 0.664, confirming that pointwise embedding mimicry is counterproductive under a $26\times$ gap.

Coupled repulsive KD overcomes the gap. Allowing λ_{KL} to decay into negative values ($r=-0.8$) improves HC18 to 84.4%, surpassing the teacher’s 83.5% (Figure 2b), and boosts F1-3Brain from 0.715 to 0.763.

Selective Repulsive KD achieves the best results. Diagonal protection with NCKD amplification ($\beta_0=2$, $r=-0.8$) surpasses the teacher on HC18 (88.6% vs. 83.5%) and F1-3Brain (0.784 vs. 0.702). Comparing selective against coupled isolates diagonal protection’s contribution: HC18 +4.2 pp, F1-3Brain +2.1 pp. The larger HC18 gain suggests that diagonal protection is particularly important for retrieval-dependent tasks that rely on preserved image-text associations, whereas classification benefits more from the repulsive signal itself. Higher amplification ($\beta_0\geq 4$) and weaker repulsion ($r\geq -0.5$) both degrade performance, confirming that the decomposition and repulsion strength jointly determine the result. Across three seeds (42, 123, 7), the best selective configuration yields Avg.[‡] 0.867 ± 0.016 , with HC18 validity $87.1\pm 2.2\%$ and F1-3Brain exhibiting the highest variance (0.735 ± 0.069); all seeds surpass the static KD baseline (supplementary § 3.3).

4.5 Training Dynamics

Figure 2 visualises training behaviour across KD configurations. Repulsive runs exhibit a characteristic “late surge” in zero-shot performance once the KD weight crosses zero (\sim epoch 11 for $r=-0.8$), with Selective Repulsive KD ($\beta_0=2$, $r=-0.8$) reaching the highest Avg.[‡] (0.886), exceeding the teacher’s 0.853. The surge occurs because the sign flip converts the KD objective from minimising to maximising KL divergence on non-target pairs: the inverted gradient directly penalises the student for preserving the teacher’s inter-class confusion structure, forcing rapid discovery of more discriminative features. Extended dynamics are in supplementary Figs. S4–S5.

4.6 Feature Space Analysis

t-SNE Visualisation. Figure 3 shows t-SNE projections of brain sub-plane embeddings, the hardest subtask (three visually similar fetal head planes). Without KD, transthalamic and transventricular overlap substantially; static KD provides marginal improvement. Selective Repulsive KD produces dramatically tighter, well-separated clusters, consistent with the +8.2 pp F1-3Brain gain over the teacher.

Table 3: Unified ablation: KD strategies for MobileFetalCLIP (FastViT-MC10, 11.4M visual encoder) distilled from FetalCLIP ViT-L/14 (304M). All runs: lr= 10^{-5} , $\tau_{KD}=5.0$, seed 42, 20 epochs. Best per-column in **bold**. Avg.[‡]: run-selection heuristic (F1-all + HC18%/100)/2.

Configuration	F1-5Plane	F1-3Brain	F1-all	HC18 (%)	Avg. [‡]
<i>FetalCLIP Teacher (ViT-L/14)</i>	<i>0.973</i>	<i>0.702</i>	<i>0.871</i>	<i>83.5</i>	<i>0.853</i>
No KD (CLIP only)	0.889	0.712	0.823	71.3	0.768
Static KD ($\lambda_{KL}=1.0$)	0.946	0.715	0.860	79.4	0.826
Static + Feat. KD ($\lambda_{feat}=2000$)	0.946	0.664	0.840	75.9	0.800
Pos. Decay ($\lambda_{KL}: 1 \rightarrow 0.1$)	0.902	0.713	0.831	74.6	0.788
Full Decay ($\lambda_{KL} \rightarrow 0$)	0.842	0.742	0.805	73.1	0.768
Conf. Penalty ($\varepsilon=0.1$)	0.854	0.680	0.789	74.9	0.769
<i>Coupled Repulsive KD (uniform λ_{KL} on full matrix)</i>					
$r=-0.8$	0.933	0.763	0.869	84.4	0.857
<i>Selective Repulsive KD (diag.-protected, off-diag. repulsion)</i>					
Selective $\beta_0=2, r=-0.8$	0.946	0.784	0.885	88.6	0.886
<i>NCKD amplification ablation (selective, $r=-0.8$):</i>					
$\beta_0=4$	0.950	0.709	0.860	85.4	0.857
$\beta_0=8$	0.943	0.714	0.857	78.6	0.822
<i>Repulsion strength ablation (selective, $\beta_0=2$):</i>					
$r=-0.5$	0.941	0.725	0.860	84.6	0.853
$r=-0.4$	0.938	0.724	0.858	78.4	0.821

Table 4: Embedding geometry on Planes DB (5-plane, 8,187 images). d_{eff} : effective dimensionality (participation ratio). Rank₉₅: singular values for 95% variance.

Method	d_{eff}	Rank ₉₅	Silh. \uparrow	Intra \uparrow	Inter \downarrow	Unif. \downarrow
Static KD ($\lambda_{KL}=1.0$)	8.0	77	0.375	0.712	0.445	-1.662
Conf. penalty	9.0	84	0.406	0.693	0.389	-1.811
Coupled $r=-0.8$	6.4	50	0.509	0.645	0.010	-2.231
Selective $\beta_0=2$	10.0	74	0.525	0.623	0.076	-2.308

Embedding Geometry. We perform quantitative cluster and spectral analysis on the Planes DB 5-plane evaluation set (8,187 images). Table 4 reports silhouette score, inter-class cosine similarity, Wang and Isola’s uniformity [32], and effective dimensionality d_{eff} via the participation ratio of the embedding covariance spectrum.

Repulsive KD dramatically improves cluster geometry: silhouette scores increase by +40% over static KD (0.525 vs. 0.375), and inter-class cosine collapses from 0.445 to near zero. The confidence penalty provides only modest improvement (0.406), confirming that undirected entropy cannot match teacher-informed repulsion. Coupled repulsion concentrates features into fewer dimensions (d_{eff} 6.4 vs. 8.0 for static KD), while Selective Repulsive KD achieves the highest d_{eff} (10.0) and best uniformity (-2.308), connecting to the Barlow Twins [36] decorrelation principle. Full spectral analysis is in supplementary § 2.6.

Per-class F1 heatmaps and confusion matrices are in supplementary § 2.1.

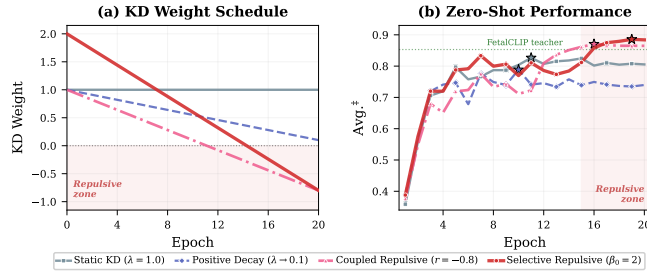


Fig. 2: Training dynamics for representative KD configurations. **(a)** KD weight schedule over epochs: for coupled runs the weight is $\lambda_{\text{KL}}(t)$; for selective mode it is $\beta(t)$. Positive decay stays above zero; repulsive variants cross into the repulsive zone (weight < 0). **(b)** Zero-shot Avg. \dagger per epoch: repulsive runs exhibit a characteristic late surge once entering the repulsive zone; Selective Repulsive KD ($\beta_0=2$, $r=-0.8$) achieves the highest final score (\star), exceeding the FetalCLIP teacher.

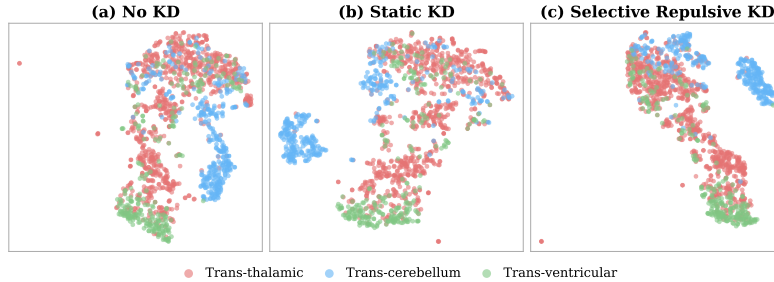


Fig. 3: t-SNE projections of brain sub-plane embeddings (transthalamic, transcerebellum, transventricular). **(a)** No KD: overlapping clusters. **(b)** Static KD: marginal improvement. **(c)** Selective Repulsive KD: well-separated, compact clusters.

4.7 Linear Probing Evaluation

To assess frozen feature quality independently of the contrastive alignment used in zero-shot evaluation, we conduct linear probing on three downstream tasks (Tab. 5). For each task, we freeze the image encoder, extract L2-normalised features, and train a single linear layer.

Setup. *6-view plane classification* and *3-class brain sub-plane classification* use Planes DB [5] with the original patient-level train/test split (7,129/5,271 for 6-view; 1,543/1,406 for brain). *Congenital heart disease (CHD) detection* uses 418 four-chamber fetal heart ultrasound videos (161 normal, 257 abnormal) with patient-stratified split (333/85); for each video, 16 frames are sampled, frame-wise features extracted and concatenated before classification. All experiments use 5-fold cross-validation with 5 seeds (25 runs); 95% confidence intervals are computed via Student’s t -distribution.

Results. MobileFetalCLIP retains 97–98% of the FetalCLIP teacher’s linear probing performance across all three tasks, while substantially outperforming

Table 5: Linear probing evaluation. Frozen encoder features + single linear layer. 95% CIs from 5-fold \times 5 seeds. MobileFetalCLIP retains 97–98% of the teacher’s performance at 26 \times fewer visual parameters.

Model	6-View (F1)	Brain (F1)	CHD (AUROC)
CLIP (ViT-L/14)	.867 (.866–.869)	.634 (.632–.637)	.679 (.650–.708)
BiomedCLIP (ViT-B/16)	.856 (.855–.858)	.582 (.577–.588)	.643 (.622–.665)
UniMed-CLIP (ViT-B/16)	.860 (.858–.861)	.607 (.603–.610)	.718 (.702–.734)
FetalCLIP (ViT-L/14)	.947 (.947–.948)	.820 (.818–.822)	.787 (.770–.804)
MobileFetalCLIP (FastViT)	.930 (.930–.931)	.799 (.797–.800)	.769 (.758–.779)
<i>Retention</i>	<i>98.2%</i>	<i>97.4%</i>	<i>97.7%</i>

all general-purpose VLMs (+6–22 pp on 6-view, +17–22 pp on brain sub-plane, +5–13 pp on CHD). The gap is expected: linear probing measures frozen feature information content, bounded by encoder capacity [25], whereas zero-shot evaluation probes image-text alignment, which logit-based distillation transfers most effectively [11, 19]. This explains why MobileFetalCLIP surpasses the teacher on zero-shot tasks while retaining near-teacher linear probing.

5 Discussion

5.1 When and How Does Selective Repulsive KD Work?

Selective Repulsive KD outperforms standard KD when the capacity gap is large enough that faithful mimicry wastes student capacity. In our 26 \times setting, the controlled ablation (coupled vs. selective, both $r=-0.8$) confirms that diagonal protection accounts for +4.2 pp in HC18 and +2.1 pp in F1-3Brain (Sec. 4.4).

The mechanism is *structured decorrelation*: well-separated, confident student representations that are systematically different from the teacher’s. Three lines of evidence support this:

1. Embedding geometry (Tab. 4): silhouette +40% over static KD, near-zero inter-class cosine, highest d_{eff} (10.0) and best uniformity (−2.308); see supplementary § 2.6 for spectral analysis.

2. Logit distributions (supplementary § 2.2): classification entropy drops from 1.248 to 0.167 (more confident), while teacher-student rank correlation remains high (0.822), indicating preserved relational structure with divergence in specific decisions.

3. Per-class patterns (supplementary § 2.1): brain sub-plane F1 reaches 0.784 (+8.2 pp over teacher), confirming superior fine-grained discrimination when freed from the teacher’s non-target structure.

Why can the student surpass the teacher? The teacher’s ViT-L/14 distributes representational capacity across all inter-class relationships through global self-attention, including confusable pairs (*e.g.* brain sub-planes sharing similar ultrasound textures). The compact FastViT student (11.4M visual parameters) cannot afford such distributed representations; standard KD wastes capacity forcing the student to approximate inter-class relationships it cannot

faithfully reproduce. Selective Repulsive KD uses the teacher’s confusion patterns as a structured signal for *where* to build sharper boundaries, allowing the student to exploit its convolutional-attention architecture for local discriminative cues that the teacher’s global attention did not prioritise.

5.2 When Does It Fail?

Excessive repulsion causes collapse. An exploration-phase coupled run with $r=-1.6$ collapsed after epoch 14; excessive NCKD amplification ($\beta_0=8$) degrades HC18 to 78.6%. All successful repulsive schedules require an initial attractive phase to absorb domain knowledge before diverging. Feature KD ($\lambda_{\text{feat}}=2000$) consistently degrades performance under our $26\times$ gap (HC18: 79.4% \rightarrow 75.9%), as the teacher’s embedding space is too different for pointwise alignment.

5.3 Connections to Prior Work

Selective Repulsive KD draws from the capacity gap literature [7, 18, 25], Zhao *et al.*’s [39] decomposition insight (our contrastive adaptation differs; supplementary § 2.4), Barlow Twins [36] decorrelation, and Born-Again Networks [8]; our confidence penalty ablation empirically distinguishes it from undirected entropy regularisation [20].

5.4 Limitations and Future Work

While retrospective benchmarks establish strong zero-shot capabilities, clinical translation requires prospective validation to assess robustness against diverse ultrasound hardware and operator variability. Given MobileFetalCLIP’s 1.6 ms latency, our immediate focus is real-time evaluation on portable point-of-care (POCUS) devices, targeting live assistive feedback in low-resource settings. Furthermore, because Selective Repulsive KD is architecture- and domain-agnostic, future work will extend this framework to other resource-constrained clinical applications, such as echocardiography and cross-modal retrieval in general radiology.

6 Conclusion

MobileFetalCLIP applies **Selective Repulsive Knowledge Distillation**, decomposing contrastive KD into diagonal and off-diagonal terms and selectively repelling only the latter, to distill FetalCLIP into a mobile vision-language model for fetal ultrasound. With $26\times$ fewer parameters and $32\times$ fewer GMACs, MobileFetalCLIP surpasses the teacher on HC18 validity (+5.1 pp) and brain sub-plane F1 (+8.2 pp) at 1.6 ms on iPhone 16 Pro ($24\times$ faster). We release MobileFetalCLIP and the Selective Repulsive KD framework to support mobile medical AI at <https://github.com/numanai/MobileFetalCLIP>.

References

1. Apple: MobileCLIP2: Efficient image-text pretraining (2024), apple ML Research
2. Athalye, C., van Nesselrooij, A., Rizvi, S., Haak, M., Moon-Grady, A.J., Arnaout, R.: Deep-learning model for prenatal congenital heart disease screening generalizes to community setting and outperforms clinical detection. *Ultrasound in Obstetrics & Gynecology* **63**(1), 44–52 (2024). <https://doi.org/10.1002/uog.27503>
3. Baumgartner, C.F., Kamnitsas, K., Matthew, J., Fletcher, T.P., Koch, S., Kainz, L.M., Rueckert, D.: SonoNet: Real-time detection and localisation of fetal standard scan planes in freehand ultrasound. *IEEE Trans. Med. Imaging* **36**(11), 2204–2215 (2017). <https://doi.org/10.1109/TMI.2017.2712367>
4. Branwen, T., et al.: WebDataset (2021), <https://github.com/webdataset/webdataset>
5. Burgos-Artizzu, X.P., Coronado-Gutiérrez, D., Valenzuela-Alcaraz, B., Bonet-Carne, E., Eixarch, E., Crispi, F., Gratacos, E.: Evaluation of deep convolutional neural networks for automatic classification of common maternal fetal ultrasound planes. *Scientific Reports* **10**(1), 10200 (2020). <https://doi.org/10.1038/s41598-020-67076-5>
6. Cherti, M., Beaumont, R., Wightman, R., Wortsman, M., Ilharco, G., Gordon, C., Schuhmann, C., Schmidt, L., Jitsev, J.: Reproducible scaling laws for contrastive language-image learning. In: *CVPR* (2023)
7. Cho, J.H., Hariharan, B.: On the efficacy of knowledge distillation. In: *ICCV* (2019)
8. Furlanello, T., Lipton, Z.C., Tschannen, M., Itti, L., Anandkumar, A.: Born again neural networks. In: *ICML* (2018)
9. Gomes, R.G., Vwalika, B., Lee, C., Willis, A., Sieniek, M., Tse, D., Mhango, J., Price, J.T., Berquist, W.R., Stringer, J.S., Kim, C.Y.: A mobile-optimized artificial intelligence system for gestational age and fetal malpresentation assessment. *Communications Medicine* **2**, 128 (2022). <https://doi.org/10.1038/s43856-022-00194-5>
10. van den Heuvel, T.L., de Bruijn, D., de Korte, C.L., van Ginneken, B.: Automated measurement of fetal head circumference using 2d ultrasound images. *PLOS One* **13**(8), e0200412 (2018)
11. Hinton, G., Vinyals, O., Dean, J.: Distilling the knowledge in a neural network. *arXiv preprint arXiv:1503.02531* (2015)
12. Huang, T., You, S., Wang, F., Qian, C., Xu, C.: Knowledge distillation from a stronger teacher. In: *NeurIPS* (2022)
13. Ilharco, G., Wortsman, M., Wightman, R., Gordon, C., Carlini, N., Taori, R., Dave, A., Shankar, V., Namkoong, H., Miller, J., Hajishirzi, H., Farhadi, A., Schmidt, L.: OpenCLIP (2021), <https://doi.org/10.5281/zenodo.5143773>
14. Khattak, M.U., Kunhimon, S., Naseer, M., Khan, S., Khan, F.S.: UniMed-CLIP: Towards a unified image-text pretraining paradigm for diverse medical imaging modalities. *arXiv preprint arXiv:2412.10372* (2024)
15. Kim, Y., Yim, J., Yun, J., Kim, J.: NLNL: Negative learning for noisy labels. In: *ICCV* (2019)
16. Kiserud, T., Piaggio, G., Carroli, G., Widmer, M., Carvalho, J., Jensen, L.N., Giordano, D., Cecatti, J.G., Aleem, H.A., Talegawkar, S.A., Benachi, A., Diemert, A., Kitoto, A.T., Thinkhamrop, A., Lumbiganon, J., Tabor, P., Perez, A.G., Hecher, R., Hanson, K., Gülmezoglu, M.A., Platt, L.D.: The World Health Organization fetal growth charts: A multinational longitudinal study of ultrasound biometric measurements and estimated fetal weight. *PLoS Medicine* **14**(1), e1002220 (2017). <https://doi.org/10.1371/journal.pmed.1002220>

17. Maani, F., Saeed, N., Saleem, T.J., Farooq, Z., Alasmawi, H., Diehl, W., Mohammad, A., Waring, G., Valappil, S., Bricker, L., Yaqub, M.: FetalCLIP: A visual-language foundation model for fetal ultrasound image analysis. arXiv preprint arXiv:2502.14807 (2025)
18. Mirzadeh, S.I., Farajtabar, M., Li, A., Levine, N., Matsukawa, A., Ghasemzadeh, H.: Improved knowledge distillation via teacher assistant. In: AAAI (2020)
19. Park, W., Kim, D., Lu, Y., Cho, M.: Relational knowledge distillation. In: CVPR (2019)
20. Pereyra, G., Tucker, G., Chorowski, J., Kaiser, L., Hinton, G.: Regularizing neural networks by penalizing confident output distributions. In: International Conference on Learning Representations Workshop (2017)
21. Radford, A., Kim, J.W., Hallacy, C., Ramesh, A., Goh, G., Agarwal, S., Sastry, G., Askell, A., Mishkin, P., Clark, J., Krueger, G., Sutskever, I.: Learning transferable visual models from natural language supervision. In: ICML (2021)
22. Romero, A., Ballas, N., Kahou, S.E., Chassang, A., Gatta, C., Bengio, Y.: FitNets: Hints for thin deep nets. In: ICLR (2015)
23. Salim, I., Goldstein, A.C., Lee, C., Miao, R., Willis, A., Leite, M., Vwalika, B., Gracia, W.V.D., Stringer, E.M., Stringer, J.S., Lindblad, R.: AI estimation of gestational age from blind ultrasound sweeps in low-resource settings. *NEJM Evidence* **1**(5) (2022). <https://doi.org/10.1056/EVIDoa2100058>
24. Slimani, S., Agour, S., Serfati, S., Aboughazil, F., Hassani, M., Khadir, Y., Laoudiyi, D., Saadi, H., Bouhya, S., Mounsif, Y., Rizk, M., Bouchkara, T., Belarbi, A., el Houda Boudjenane, N., Maoulainine, N.: Fetal biometry and amniotic fluid volume assessment end-to-end automation using deep learning. *Nature Communications* **14**, 7047 (2023). <https://doi.org/10.1038/s41467-023-42438-5>
25. Stanton, S., Izmailov, P., Kirichenko, P., Alemi, A.A., Wilson, A.G.: Does knowledge distillation really work? In: NeurIPS (2021)
26. Stewart, K.A., Navarro-Colorado, S.F., Kang, J., Piemonte, D.P., Legge, F., Wilson, J.M., Raza, H., Supriyanto, J., Ram, M.: Trends in ultrasound use in low and middle income countries: A systematic review. *International Journal of MCH and AIDS* **9**(1), 103–120 (2020). <https://doi.org/10.21106/ijma.294>
27. Sun, S., Ren, W., Li, J., Wang, R., Cao, X.: Logit standardization in knowledge distillation. In: CVPR (2024)
28. Tian, Y., Krishnan, D., Isola, P.: Contrastive representation distillation. In: ICLR (2020)
29. Tiu, E., Talius, E., Patel, P., Langlotz, C.P., Ng, A.Y., Rajpurkar, P.: Expert-level detection of pathologies from unannotated chest X-ray images via self-supervised learning. *Nature Biomedical Engineering* **6**, 1399–1406 (2022)
30. Vasu, P.K.A., Gabriel, J., Zhu, J., Tuzel, O., Ranjan, A.: FastViT: A fast hybrid vision transformer using structural reparameterization. In: ICCV (2023)
31. Vasu, P.K.A., Pouransari, H., Faghri, F., Vemulapalli, R., Tuzel, O.: MobileCLIP: Fast image-text models through multi-modal reinforced training. In: CVPR (2024)
32. Wang, T., Isola, P.: Understanding contrastive representation learning through alignment and uniformity on the hypersphere. In: ICML (2020)
33. Wang, Z., Wu, Z., Agarwal, D., Sun, J.: MedCLIP: Contrastive learning from unpaired medical images and text. In: EMNLP. pp. 3876–3887 (2022)
34. Wu, K., Peng, H., Chen, Z., Liu, M., Hu, X., Hu, H., Li, X., Fu, J., Long, M.: TinyCLIP: CLIP distillation via affinity mimicking and weight inheritance. In: ICCV (2023)
35. Yang, Y.L., Chang, Y.C., Chen, H.W., Chiu, W.C., Wang, Y.C.F.: CLIP-KD: An empirical study of CLIP model distillation. In: CVPR (2024)

36. Zbontar, J., Jing, L., Misra, I., LeCun, Y., Deny, S.: Barlow twins: Self-supervised learning via redundancy reduction. In: ICML (2021)
37. Zhai, X., Mustafa, B., Kolesnikov, A., Beyer, L.: Sigmoid loss for language image pre-training. In: ICCV (2023)
38. Zhang, S., Xu, Y., Usuyama, N., Bagga, J., Tinn, R., Preston, S., Rao, R., Wei, M., Valluri, N., Wong, C., Tupini, A., Wang, Y., Mazzola, M., Shukla, S., Liden, L., Gao, J., Lungren, M.P., Naumann, T., Wang, S., Poon, H.: BiomedCLIP: a multimodal biomedical foundation model pretrained from fifteen million scientific image-text pairs. arXiv preprint arXiv:2303.00915 (2023)
39. Zhao, B., Cui, Q., Song, R., Qiu, Y., Liang, J.: Decoupled knowledge distillation. In: CVPR (2022)